applied sciences

MDPI

Article

Study on Heat Generation Mechanisms and Circumferential Temperature Evolution Characteristics of Journal Bearings Under Different Whirl Motion

Yang Liu [1,2], Xujiang Liu [1,2], Tingting Yang [1,2] and Qi Yuan [1,2,*]

[1] School of Energy and Power Engineering, Xi'an Jiaotong University, Xi'an 710049, China; lyang1907@163.com (Y.L.); 4122303014@stu.xjtu.edu.cn (X.L.); ytt1181227696@stu.xjtu.edu.cn (T.Y.)
[2] Shaanxi Provincial Engineering Laboratory of Turbomachinery and Power Equipment, Xi'an Jiaotong University, Xi'an 710049, China
* Correspondence: qyuan@xjtu.edu.cn

Abstract

To investigate the heat-generation mechanisms of journal bearings under different whirl motion and to clarify the corresponding temperature distribution characteristics, a computational fluid dynamics-based method was developed. The model incorporates temperature-dependent lubricant viscosity and employs an unsteady dynamic-mesh updating approach based on structured grids, enabling the automatic iterative tracking of the journal center during whirl motion. A thermal-effect analysis model that accounts for journal whirl trajectories was thereby established. The whirl orbit shape is characterized using elliptical eccentricity, and the effects of whirl direction, elliptical eccentricity, and whirl frequency on the circumferential temperature and pressure distributions of the journal are examined. Results show that under forward whirl, increasing whirl frequency and elliptical eccentricity initially enhances and then weakens local hydrodynamic pressure and viscous shear dissipation in the oil-film convergent region, producing pronounced first-order circumferential temperature nonuniformity and a high risk of thermal bending at intermediate frequencies. Under backward whirl, hydrodynamic effects are reduced and heat generation shifts from localized concentration to global shear dissipation, forming a relatively uniform second-order circumferential temperature field. Increasing elliptical eccentricity causes the whirl orbit to become more linear, improving load-carrying capacity and heat-transfer performance and thereby mitigating thermally induced vibration and oil-film whirl instability.

Keywords: journal bearing; whirl motion; heat generation mechanism; circumferential temperature evolution

Check for updates

Received: 31 January 2026
Revised: 12 February 2026
Accepted: 16 February 2026
Published: 20 February 2026

Copyright: © 2026 by the authors. Licensee MDPI, Basel, Switzerland. This article is an open access article distributed under the terms and conditions of the Creative Commons Attribution (CC BY) license.

1. Introduction

Hydrodynamic journal bearings are widely used in rotor systems of turbomachinery such as steam turbines, gas turbines, and compressors, where they play a critical role in load support and vibration control. Their thermal characteristics directly affect the bearing load-carrying capacity, the minimum oil-film thickness, and overall operational reliability [1]. Under high-speed conditions, the journal often exhibits various forms of whirl motion within the bearing clearance. The associated whirl trajectories and frequencies can significantly alter lubricant flow patterns and viscous shear behavior, thereby exerting a strong influence on oil-film heat generation and circumferential temperature distributions.

Compared with steady operating conditions, the thermal behavior of journal bearings under whirl motion is characterized by pronounced nonuniformity and time-dependent features, representing a key challenge in bearing thermal analysis [2]. During whirl motion, the oil-film thickness varies periodically with time, and the convergent and divergent regions continuously migrate, leading to highly nonuniform distributions of viscous dissipation and convective heat transfer in the circumferential direction. Variations in whirl direction, orbit shape, and whirl frequency further modify the internal heat-generation mechanisms of the oil film, giving rise to distinctly different circumferential temperature patterns on the journal surface. Therefore, investigating the heat-generation mechanisms of journal bearings under different whirl motion and clarifying the corresponding temperature distribution characteristics are of great importance for improving the operational stability of high-speed rotating machinery.

Early studies on journal bearings were largely based on the isothermal assumption and the classical Reynolds equation. Such approaches can reasonably predict oil-film pressure distributions under low- and moderate-speed conditions, but they fail to capture realistic thermal behavior at high rotational speeds. With the growing recognition of thermal effects in bearing performance, the energy equation has gradually been incorporated into lubrication theory, leading to the development of thermo-hydrodynamic (THD) lubrication models. Previous studies have shown that temperature rise can markedly reduce lubricant viscosity, thereby weakening load-carrying capacity and altering frictional power loss [3]. Gomiciaga and Keogh [4] employed computational fluid dynamics to analyze flow and heat transfer within the lubricant film and found that the circumferential temperature distribution on the journal surface contains a sinusoidal component. For forward whirl orbits, the maximum temperature consistently appears upstream of the minimum oil-film thickness, whereas for backward whirl orbits, it is located downstream. Childs and Saha [5] began with stable elliptical orbits generated by initial unbalance and decomposed them into circular forward- and backward-whirl components. By calculating and superposing the corresponding temperature fields, they obtained the overall temperature distribution induced by elliptical motion. Dal et al. [6], through three-dimensional energy-equation analyses, demonstrated that radial clearance variations exert strong sensitivity on both temperature rise and load capacity: although smaller clearances enhance load support, they also lead to more complex thermal behavior. Yu et al. [7], in a comprehensive review of hydrostatic spindle systems, further emphasized that temperature-dependent viscosity plays a decisive role in thermal prediction for high-precision and high-speed applications, and neglecting this effect can significantly underestimate the temperature rise. Wang et al. [8] investigated the thermal and cavitation characteristics of elliptical bearings with different ellipticities, showing that appropriate elliptical eccentricity can effectively reduce temperature rise and improve oil-film stability. Peixoto et al. [9] analyzed the influence of isothermal and adiabatic boundary conditions in multilobe bearing systems and demonstrated that thermal boundary assumptions strongly affect the pressure distribution as well as predicted stiffness and damping. Suh and Palazzolo [10,11] developed a three-dimensional nonlinear time-varying rotor-dynamic model that incorporates temperature-dependent lubricant properties by coupling the Reynolds equation with the three-dimensional energy equation. Using the finite-element method, they established three-dimensional heat-transfer models for both the rotor and bearing and investigated the effects of thermal boundary conditions, lubricant supply temperature, initial mass unbalance, bearing support stiffness, and oil-film clearance on thermally induced vibration. Their results indicated that reducing bearing support stiffness and minimizing initial mass unbalance are effective measures for mitigating thermally induced synchronous instability. Lu et al. [12] established a thermo–fluid coupled model for gas bearings based on the compressible Reynolds equation and the

energy equation, demonstrating that temperature rise significantly influences load-carrying performance by altering gas viscosity. In a broader context of lubricated transmission systems, Skulić et al. [13] investigated the effects of lubricant viscosity grade and material factors on power losses and efficiency in worm gear transmissions. Their results showed that variations in lubricant viscosity can lead to significant differences in frictional power loss and thermal state, thereby affecting the overall system efficiency and temperature levels. Therefore, accounting for the temperature–viscosity characteristics of lubricants and their feedback on dissipative heating and temperature fields is of broad engineering relevance in the thermal analysis of hydrodynamic journal bearings.

In engineering practice, the performance of hydrodynamic journal bearings is commonly evaluated using standardized calculation procedures, such as ISO 7902-1 [14]. These standards provide design-oriented methods, based on simplified lubrication theory and empirical correlations, to estimate load capacity, minimum film thickness, friction losses, and operating temperature. However, such standardized approaches are primarily intended for steady-state operating conditions and rely on averaged quantities, steady eccentricity, and simplified thermal assumptions. Transient journal motion, complex whirl trajectories, circumferentially nonuniform temperature fields, and localized thermo-hydrodynamic coupling effects are not explicitly resolved. In particular, the influence of rotation direction, whirl frequency, and noncircular journal orbits on local heat generation and circumferential temperature evolution cannot be captured within these frameworks. Therefore, although standardized methods remain indispensable for preliminary design and engineering assessment, high-fidelity numerical approaches are still required. With the development of computational fluid dynamics (CFD) techniques, their application in bearing thermal analysis has increased steadily. Compared with conventional Reynolds-equation-based models, CFD methods can directly resolve three-dimensional flow and heat-transfer processes while simultaneously accounting for turbulence, two-phase flow, thermal boundary conditions, and complex geometries [15–17]. Taheripour et al. [15] employed a VOF two-phase model to perform transient simulations of oil–air flow and heat transfer inside industrial journal bearings, revealing that high-temperature regions are mainly concentrated in the upper oil film and near leakage paths. Rezvanpour and Miller [16] verified the physical consistency of CFD results for bearing chambers through scale analysis, providing a new approach for assessing numerical-model reliability under limited experimental conditions. In practical applications, cavitation, bubbles, and oil–gas coexistence are commonly present in bearing films and have a pronounced influence on thermal behavior and load-carrying performance. Li et al. [18] developed a bubbly lubrication model based on multiphase mixture theory and demonstrated experimentally that thermal effects exert a much stronger influence on bearing performance than interfacial effects. Wei et al. [19] further incorporated bubble-dynamics equations, revealing the modulation mechanism of bubble evolution on temperature-field distributions. Sun et al. [20] investigated the coupled effects of journal whirl and cavitation using three-dimensional CFD combined with dynamic-mesh techniques, showing that increasing whirl frequency intensifies oil-film-force fluctuations and rapidly degrades system stability. Bhat et al. [21,22] demonstrated through CFD analyses that active or passive thermal-management designs—such as deep-groove structures, cooling channels, and surface texturing—can effectively reduce local hot spots and thermal deformation. Li et al. [23] used CFD to investigate the static and dynamic characteristics of tilting-pad bearings and developed a new dynamic-mesh algorithm that preserves mesh topology during updating, making it particularly effective for large journal perturbations. Hagemann et al. [24] combined CFD and experimental analysis to study secondary flow outside the lubrication clearance in tilting-pad radial bearings, as well as the conjugate heat transfer between fluid and solid components. Yang and Palazzolo [25,26]

established CFD-based models of tilting-pad journal bearings and incorporated bidirectional fluid–structure interaction to account for thermal deformation of both shaft and pads, thereby eliminating uncertain mixing coefficients in Reynolds-based models and improving temperature-prediction accuracy. Subsequently, Yang and Palazzolo [27,28] integrated CFD with convolutional neural networks (CNNs), demonstrating strong predictive capability for bearing temperature distributions. They further replaced full CFD solvers with finite-volume-based surrogate models [29,30], significantly accelerating computation while improving prediction accuracy and efficiency through machine-learning techniques. Gheller et al. [31] employed parameterized geometries and mesh strategies to avoid dynamic-mesh formulations in CFD models, thereby accelerating the design process, reducing computational cost, and incorporating heat exchange between the lubricant and rotating shaft to enhance prediction accuracy. Xia et al. [32] investigated the transient hydrodynamic forces and adaptive pad motion of hybrid porous tilting-pad bearings and, using CFD-based fluid–structure interaction models, evaluated the effects of eccentricity, rotor speed, supply pressure, pivot stiffness, and damping on pad adaptation behavior and rotor dynamic coefficients.

During actual operation, rotor motion is influenced by factors such as rotational speed, applied load, rotor unbalance, and lubrication conditions, and therefore cannot be described by a simple elliptical whirl trajectory. However, most existing studies have focused on steady-state or simplified whirl conditions, and a systematic understanding of how heat-generation mechanisms evolve and how circumferential temperature fields form under different whirl motion remains lacking. In this work, a journal bearing was taken as the research object. Focusing on the motion characteristics of the journal under different whirl motion, an unsteady transient hydrodynamic model based on a dynamic-mesh approach was developed. The shape of the journal whirl trajectory was characterized using elliptical eccentricity, and the effects of different elliptical eccentricities and whirl frequencies under forward and backward whirl conditions on oil-film heat-generation mechanisms and circumferential temperature evolution were systematically investigated. The present study provides a theoretical basis for thermal analysis and stability-related research of journal bearings.

2. Governing Equations and Numerical Method

2.1. Governing Equations of Computational Fluid Dynamics

In this study, the lubricant was treated as an incompressible Newtonian fluid with temperature-dependent properties. The flow, heat transfer, and turbulence can be described by solving the governing equations. Turbulence was modeled using the Reynolds-averaged Navier–Stokes (RANS) equations, which are derived through a statistical averaging procedure. The incompressible Reynolds-averaged continuity, momentum, and energy equations are given below. The continuity equation is [33]:

$$\frac{\partial \rho}{\partial t} + \frac{\partial}{\partial x_i}(\rho u_i) = 0 \tag{1}$$

where ρ is the density of the lubricating oil, u_i is the fluid velocity component, and t denotes time.

The momentum equation is given by:

$$\frac{\partial \rho u_i}{\partial t} + \frac{\partial}{\partial x_j}(\rho u_i u_j) = -\frac{\partial p'}{\partial x_i} + \frac{\partial}{\partial x_j}\left[\mu\left(\frac{\partial u_i}{\partial x_j} + \frac{\partial u_j}{\partial x_i}\right)\right] + S_M \tag{2}$$

where u_i and u_j are the velocity components in the i- and j-directions, respectively; p' is the modified pressure that incorporates the isotropic part of the Reynolds stresses; μ is the dynamic viscosity; and S_M denotes the momentum source term, representing additional body forces or momentum corrections introduced by numerical models, such as rotating-reference-frame effects or dynamic-mesh motion.

Given the incompressible nature of the lubricant and the low-Mach-number flow conditions, the energy equation is expressed in terms of temperature. The viscous dissipation term is included to account for shear-induced heat generation within the lubricant film, which plays a dominant role in the thermal behavior of journal bearings. Solving the energy equation yields the three-dimensional temperature field of the oil film [34]:

$$\rho c_p \left(\frac{\partial T}{\partial t} + u_i \frac{\partial T}{\partial x_i} \right) = \frac{\partial}{\partial x_i} \left(k \frac{\partial T}{\partial x_i} \right) + \Phi \tag{3}$$

$$\Phi = \mu \left(\frac{\partial u_i}{\partial x_j} + \frac{\partial u_j}{\partial x_i} \right) \frac{\partial u_i}{\partial x_j} \tag{4}$$

where c_p is the specific heat capacity at constant pressure; T is the lubricant temperature; k is the thermal conductivity; and Φ denotes the viscous dissipation term, representing the conversion of mechanical energy into thermal energy induced by velocity gradients.

During rotor motion, viscous shear within the oil film generates dissipation heat, leading to a temperature rise that in turn reduces the lubricant viscosity. Therefore, the influence of temperature on the lubrication characteristics of journal bearings must be considered. In this study, the Reynolds temperature–viscosity model [10] was adopted:

$$\mu = \mu_0 e^{\alpha_\mu (T - T_0)} \tag{5}$$

where T_0 is the lubricant supply temperature, μ_0 is the initial dynamic viscosity of the lubricant, and α_μ is the temperature–viscosity index.

In high-speed journal bearings, the oil-film pressure varies rapidly in the circumferential direction. When the local pressure drops below the saturated vapor pressure of the lubricant, film rupture may occur, leading to the formation of cavitation regions. This phenomenon has a pronounced influence on load-carrying characteristics, shear-dissipation distribution, and temperature-field structure, and therefore must be considered in numerical modeling. In the present study, incompressible multiphase flow, thermo-fluid coupling, and turbulence were all incorporated into the fluid-domain model. For cavitating multiphase flow, a mixture model based on the Euler–Euler approach was adopted. Phase change between the liquid and vapor phases mainly occurs in the divergent region of the oil film or in areas with insufficient lubricant supply. Based on the Rayleigh–Plesset model, the mass-transfer equation is derived, and the continuity equation for phase α can be expressed as:

$$\frac{\partial}{\partial t}(r_\alpha \rho_\alpha) + \frac{\partial}{\partial x_i}(r_\alpha \rho_\alpha u_{\alpha i}) = \dot{m}_\alpha \tag{6}$$

The mass-transfer equations for evaporation and condensation [25] are given, respectively, as:

$$\dot{m}_v = C_{F,evap} \frac{3 r_{nuc} r_l \rho_l}{R_{bb}} \sqrt{\frac{2}{3\rho_l}(p_{cav} - p)} \tag{7}$$

$$\dot{m}_l = C_{F,cond} \frac{3 r_v \rho_v}{R_{bb}} \sqrt{\frac{2}{3\rho_l}(p - p_{cav})} \tag{8}$$

where $\dot{m}_v$ and $\dot{m}_l$ are the mass-transfer rates of evaporation and condensation, respectively; $C_{F,evap}$ is the empirical evaporation coefficient, taken as 50; $C_{F,cond}$ is the empirical condensation coefficient, taken as 0.01; R_{bb} is the bubble radius, taken as 2 nm; r_{nuc} is the volume fraction of nucleation sites, taken as 5×10^{-4}; r_l and r_v are the volume fractions of the liquid and vapor phases, respectively; and p_{cav} is the cavitation pressure. The remaining parameters in the mass-transfer model were obtained using the default settings of the CFD solver.

The RANS equations introduce Reynolds stresses, which represent additional unknowns and therefore require supplementary closure equations. The SST k–ω turbulence model is a two-equation eddy-viscosity model that employs the k–ω formulation in the inner region of the boundary layer and can be directly applied near the wall, including the viscous sublayer. The transport equations for the turbulent kinetic energy k and the specific dissipation rate ω are given in Equations (9) and (10). Within the bearing clearance, the flow is primarily governed by near-wall shear and pressure gradients. Due to journal rotation and its interaction with the incoming lubricant jet, localized flow separation and transient phenomena may occur. Compared with the standard laminar model and other turbulence models, the SST k–ω model provides higher accuracy in resolving near-wall effects, enabling more reliable prediction of the hydrodynamic pressure distribution [25].

$$\frac{\partial}{\partial t}(\rho k) + \frac{\partial}{\partial x_i}(\rho u_i k) = \frac{\partial}{\partial x_i}\left[\left(\mu + \frac{\mu_t}{\sigma_{k3}}\right)\frac{\partial k}{\partial x_i}\right] + P_k - \beta^{'}\rho k\omega \tag{9}$$

$$\frac{\partial}{\partial t}(\rho \omega) + \frac{\partial}{\partial x_i}(\rho u_i \omega) = \frac{\partial}{\partial x_i}\left[\left(\mu + \frac{\mu_t}{\sigma_{\omega 3}}\right)\frac{\partial \omega}{\partial x_i}\right] + (1 - B_1)2\rho\frac{1}{\sigma_{\omega 2}\omega}P_k - \beta_3\rho\omega^2 \tag{10}$$

where $\beta' = 0.09$; $\sigma_{\omega 2} = 1/0.856$; the coefficients σ_{k3}, $\sigma_{\omega 3}$, and β_3 are obtained by linear interpolation between two sets of model constants using the blending function B_1, i.e., $\phi_3 = B_1\phi_1 + (1 - B_1)\phi_2$; the left-hand side of the k–ω transport equations represents the unsteady accumulation and convective transport of turbulent kinetic energy and specific dissipation rate, respectively; turbulent diffusion is governed by the eddy viscosity μ_t and the model coefficients σ_{k3} and $\sigma_{\omega 3}$; P_k denotes the production of turbulent kinetic energy induced by mean velocity shear; $-\beta'\rho k\omega$ and $-\beta_3\rho\omega^2$ are the dissipation terms of k and ω, respectively; $(1 - B_1)2\rho(\sigma_{\omega 2}\omega)^{-1}P_k$ is the coupling term, which regulates the evolution of the turbulent time scale across different regions through the blending function.

2.2. Journal Dynamic Equations

To clarify the force–motion relationship of the journal under unbalance excitation, a dynamic analysis of the journal was performed. The equations of motion for the journal center in the hydrodynamic bearing are given as follows:

$$\begin{cases} M\frac{\partial^2 x}{\partial t^2} = F_x + Me\omega^2\cos\ \omega t \\ M\frac{\partial^2 y}{\partial t^2} = F_y + Me\omega^2\sin\omega t - Mg \end{cases} \tag{11}$$

where M is the effective journal mass supported by the bearing; e is the mass eccentricity of the journal; ω is the rotational speed of the rotor; and F_x and F_y are the oil-film force components in the x- and y-directions, respectively.

Figure 1 illustrates the schematic of the journal bearing model, where O denotes the bearing center, O_j the journal center, and O_m the mass center of the journal. By solving the journal equations of motion, the static equilibrium position of the journal can be obtained. When synchronous whirl occurs, a point on the journal surface rotates about the shaft axis with angular velocity ω, while the journal center simultaneously whirls around its static equilibrium position at the same speed. Under this condition, there exists a location on the journal surface where the oil-film thickness remains minimum throughout the

motion. The oil-film temperature at this location is therefore the highest, forming a "hot spot". Correspondingly, the location with the lowest temperature is referred to as the "cold spot", and the temperature difference between the hot and cold spots is defined as the circumferential temperature difference of the journal. The high spot corresponds to the location where the journal surface is closest to the bearing. In general, the hot spot lags behind the high spot, and the phase lag angle is dependent on the rotational speed ω [35].

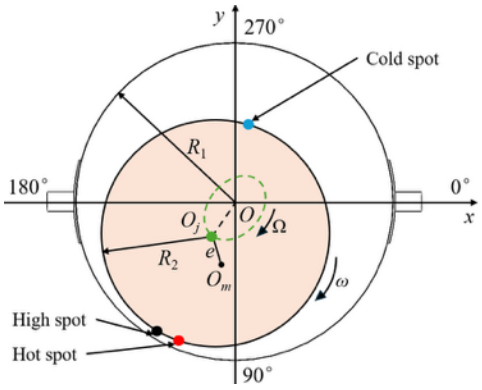

Figure 1. Schematic diagram of the journal bearing model.

2.3. Journal Whirl Orbit Equation

In high-speed rotor–bearing systems, the journal often exhibits periodic whirl motion under the action of oil-film forces, and its center trajectory may take the form of circular or elliptical closed orbits. To quantitatively characterize the spatial motion of the journal within the bearing clearance under different whirl motion, a parametric representation of the journal whirl orbit was established in this study. The journal whirl trajectory can be expressed using a complex formulation. Assuming that the initial phase angle of the whirl motion is zero and denoting the complex variable as P, the combined motion of forward and backward whirl at the same whirl frequency can be written as:

$$P = A\mathrm{e}^{i\Omega t} + B\mathrm{e}^{-i\Omega t} = x + iy \tag{12}$$

where A and B are constant complex numbers, $i = \sqrt{-1}$. Let $A = a_1 + ia_2$ and $B = b_1 + ib_2$; substituting these into the above expression yields:

$$\begin{bmatrix} x \\ y \end{bmatrix} = \begin{bmatrix} a_1 + b_1 & b_2 - a_2 \\ a_2 + b_2 & a_1 - b_1 \end{bmatrix} \begin{bmatrix} \cos(\Omega t) \\ \sin(\Omega t) \end{bmatrix} \tag{13}$$

When the journal undergoes forward whirl in the x-direction, setting $a_2 + b_2 = a$, $b_2 - a_2 = b$, $a_1 + b_1 = 0$ and $a_1 - b_1 = 0$, the forward-whirl equation of the journal motion in the x-direction can be written as:

$$\begin{cases} x = b\ \sin(\Omega t) \\ y = a\ \cos(\Omega t) \end{cases} \tag{14}$$

When the journal undergoes backward whirl in the y-direction, setting $a_1 + b_1 = a$, $a_1 - b_1 = \mathrm{b}$, $a_2 + b_2 = 0$ and $b_2 - a_2 = 0$, the backward-whirl equation of the journal motion in the y-direction is obtained as:

$$\begin{cases} x = a\ \cos(\Omega t) \\ y = b\ \sin(\Omega t) \end{cases} \tag{15}$$

where a and b denote the semi-minor and semi-major axes, respectively, of the elliptical whirl orbit, as shown in Figure 2.

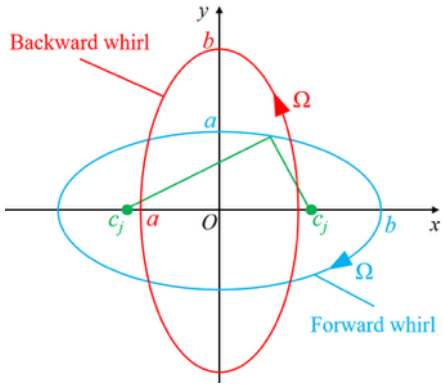

Figure 2. Schematic diagram of the journal whirl orbit.

The above whirl-orbit equation is imposed as a geometric constraint on the journal motion and incorporated into the dynamic-mesh updating procedure of the computational fluid dynamics model, thereby enabling the simulation of the periodic motion of the journal center under whirl conditions. To investigate the journal temperature distribution characteristics under different whirl trajectories and whirl frequencies, the elliptical eccentricity ε_ω was introduced to describe the orbit shape. The ellipse has a focal distance c_j, as illustrated in Figure 2. The elliptical eccentricity is defined as:

$$c_j^2 = b^2 - a^2 \tag{16}$$

$$\varepsilon_w = \frac{\sqrt{b^2 - a^2}}{b} \tag{17}$$

To ensure that the journal whirl remained within the small-perturbation regime and to avoid significant disturbance to the fundamental load-carrying structure of the oil film, the whirl amplitude was limited to less than 10% of the radial clearance [36]. Accordingly, the semi-major axis of the elliptical whirl orbit was fixed at b = 10 μm. This setting satisfies the basic small-perturbation assumption commonly adopted in bearing dynamics and ensures good comparability of the oil-film structure under different whirl frequencies and orbit shapes, thereby facilitating the identification of the intrinsic influence of whirl-state variation on bearing thermal effects. The corresponding elliptical eccentricities are listed in the following Table 1.

Table 1. Elliptical eccentricity of whirl orbits.

Elliptical Eccentricity ε_ω	a (μm)	b (μm)
0	10.0	10.0
0.2	9.8	10.0
0.4	9.2	10.0
0.6	8.0	10.0
0.8	6.0	10.0
1.0	0.0	10.0

3. Computational Model and Method

3.1. Physical Model and Dynamic Mesh Updating Method

The bearing investigated in this study was a hydrodynamic journal bearing, in which the load-carrying capacity is entirely provided by the hydrodynamic pressure generated by journal rotation. Lubricant is supplied through oil inlet holes on both sides of the bearing. A schematic of the bearing model is shown in Figure 3. Table 2 lists the material properties of the journal bearing and the lubricant. The present work focuses on the mechanisms by

which whirl motion affects hydrodynamic pressure generation and the oil-film temperature field. A comparative study of different viscosity grades has not yet been conducted, and further evaluations based on multiple lubricants will be carried out in future work. Based on the bearing parameters in Table 2 [10], a three-dimensional computational fluid dynamics model was established.

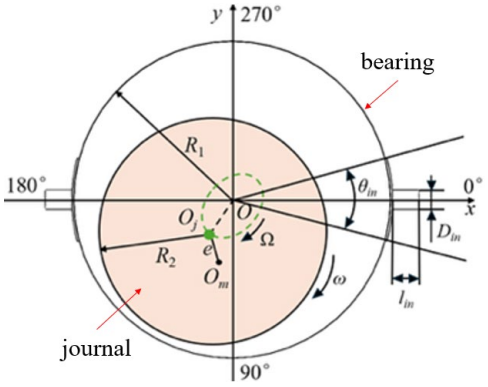

Figure 3. Schematic of the journal bearing structural parameters.

Table 2. Physical properties of the journal bearing and lubricating oil.

Parameter	Value
Bearing radius R_1 (mm)	50.9
Journal radius R_2 (mm)	50.8
Radial clearance c (mm)	0.1
Circumferential angle of the oil inlet groove θ_{in} (°)	30
Thickness of the oil inlet groove d_c (mm)	3
Length of the oil inlet hole l_{in} (mm)	8.5
Diameter of the oil inlet hole D_{in} (mm)	6
Lubricant grade	VG32 [25]
Bearing width D (mm)	50.8
Dynamic viscosity μ (kg/m·s)	0.0203
Temperature–viscosity coefficient α_μ	0.031
Supply-oil temperature T_0 (°C)	50
Density ρ (kg/m^3)	860
Specific heat capacity c_p (J/kg·°C)	2000
Thermal conductivity k (W/m·°C)	0.13
Cavitation pressure p_{cav} (Pa)	-9.00×10^4
Supply-oil pressure p_{in} (Pa)	1.32×10^5

To ensure the feasibility of the numerical model and to focus on the dominant effects of whirl states on oil-film heat generation and circumferential temperature distribution, the following assumptions and limitations were adopted in this study:

(1) Fluid compressibility and density variation: The lubricant was treated as an incompressible Newtonian fluid with constant density; pressure-induced volumetric elasticity effects were neglected.
(2) Geometry and structural deformation: The journal and bearing were assumed to be rigid bodies. Elastic deformation of the journal and flexibility of the bearing shell were not considered, nor was thermal expansion of the journal or bearing.
(3) Thermal boundaries and heat transfer model: Heat transfer on the solid side was represented by prescribed convective heat-transfer coefficients.
(4) Turbulence modeling: The flow was modeled using the RANS SST k–ω turbulence model. Transitional flow and local relaminarization effects were only approximated by the model; high-fidelity approaches such as DNS or LES were not employed.

(5) Material properties and temperature–viscosity relation: The temperature dependence of lubricant viscosity is described by the Reynolds temperature–viscosity relation. Shear-thinning behavior, pressure–viscosity effects, and non-Newtonian characteristics were neglected.
(6) Lubricant supply boundaries and oil-supply details: The supply pressure and supply temperature were specified as constant boundary conditions.

The errors introduced by the above modeling assumptions mainly affect the accurate prediction of local peak values or absolute magnitudes, but they do not alter the main conclusions of this study regarding the effects of different whirl states, frequencies, and orbit geometries on the mechanisms of oil-film heat generation and circumferential temperature distribution.

3.2. Boundary Conditions

The boundary conditions for the fluid-domain model of the journal bearing are shown in Figure 4. At the lubricant inlet, the supply pressure was set to $p_{in} = 1.32 \times 10^5$ Pa and the supply temperature to $T_0 = 50$ °C. At the outlet boundary, the outlet pressure was specified as $p_{out} = 0$ Pa and the outlet temperature as $T_{out} = 27$ °C. The inner surface of the oil film was defined as a moving wall, with its motion controlled jointly by the Fluent user-defined functions (UDFs) DEFINE_CG_MOTION and DEFINE_PROPERTY. The outer surface of the oil film was defined as a stationary wall. Both the moving and stationary walls were treated as no-slip boundaries, with a convective heat transfer coefficient of $h_c = 50$ W/m^2·°C and an ambient temperature of $T_v = 27$ °C. Together with the governing equations, these boundary conditions establish a clear and effective mathematical model for the transient thermo-hydrodynamic problem of the journal bearing.

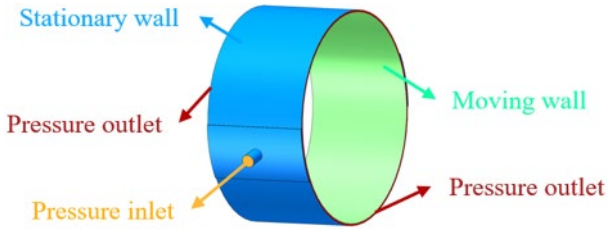

Figure 4. Boundary conditions of the journal bearing.

Based on the inlet conditions and the linear velocity of the journal, the Reynolds number at the lubricant inlet was calculated to be 5594, indicating that the flow within the bearing is very likely turbulent. The Reynolds number is calculated as follows:

$$Re = \frac{\rho U d_c}{\mu} \tag{18}$$

The SST k–ω turbulence model was adopted, and viscous dissipation was included. To control numerical accuracy, the convergence residuals for the continuity and momentum equations were set to 1×10^{-6}. The stationary wall was defined as the outer surface of the oil film, and the moving wall as the inner surface. Dynamic-mesh updating of the fluid domain was controlled using Fluent user-defined functions (UDFs). Within the DEFINE_CG_MOTION macro, the oil-film pressure obtained from the transient flow-field solution was integrated to determine the oil-film force acting on the rotor. The transient oil-film force and rotor parameters were then substituted into Equation (11) to compute the accelerations of the journal center in the x and y directions for the current time step, from which the journal-center velocity is updated. Because the journal undergoes whirl motion, the journal center varies continuously, and the rotational speed of the journal surface cannot be prescribed directly. Therefore, in the DEFINE_PROPERTY macro, the x- and y-direction

velocities of the journal surface are specified; these are vectorially combined to obtain the journal surface rotational velocity. The DEFINE_CG_MOTION macro then yields the time histories of the journal-center coordinates in the x and y directions.

During journal whirl, the computational fluid domain evolves continuously over time. However, because the radial clearance in sliding-bearing lubrication flow is extremely small while the circumferential journal velocity is high, conventional dynamic-mesh updating methods can lead to significant grid distortion and even generate negative cell volumes. To address this issue, a novel unsteady structured dynamic-mesh technique was adopted for journal-motion computation in this study. This method is based on a structured mesh in which the nodes in the fluid domain move according to a prescribed rule as the journal moves, while the mesh topology remains unchanged. As a result, high mesh quality is maintained throughout the computation, as illustrated in Figure 5.

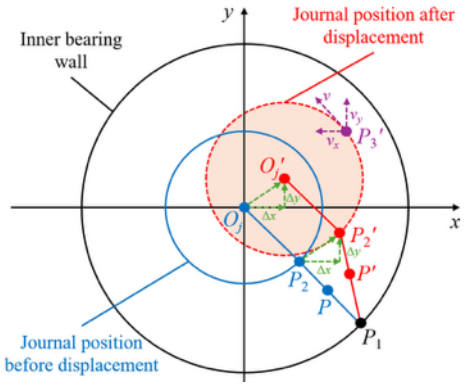

Figure 5. Schematic of dynamic-mesh updating for journal motion.

O_j denotes the current position of the journal center, and O_j' is the journal-center position at the next time step, with a displacement of Δs (Δx, Δy, 0). Let P_2 be a mesh node on the journal surface. When the journal moves by Δs, the coordinates of P_2' are given by:

$$\begin{aligned} x_{P_2'} &= x_{P_2} + \Delta x \\ y_{P_2'} &= y_{P_2} + \Delta y \end{aligned} \tag{19}$$

Let P be an arbitrary mesh node on the line segment P_1P_2, where P_1 lies on the stationary wall and P_2 lies on the journal surface. The displacement of node P is then:

$$\begin{aligned} x_{P'} &= x_P + \frac{N_i}{N}\Delta x \\ y_{P'} &= y_P + \frac{N_i}{N}\Delta y \end{aligned} \tag{20}$$

where N is the total number of grid nodes across the clearance, and N_i is the index of the node counted from the outer wall, ranging from 0~N.

Figure 6 shows the schematic flowchart for the transient journal-motion calculation. First, the initial motion parameters of the rotor are specified, and the whirl-orbit operating parameters of the journal are obtained using Table 1. The oil-film pressure from the transient flow-field computation is integrated to determine the oil-film force acting on the rotor. Based on the operating parameters of different whirl orbits, the velocity and displacement of the journal center in the x- and y-directions are calculated. Fluent then reads the relevant boundary conditions through user-defined functions (UDFs), updates the dynamic mesh of the bearing lubrication domain, and assigns the rotational velocity on the journal surface. Subsequently, the computation proceeds to the next time step, and the process iterates until the solution is completed. The computational fluid dynamics simulations in this study were performed using ANSYS Fluent, version Fluent 2021 R2.

An ANSYS Academic Research License was employed, managed through the university license server. All simulations were conducted on a high-performance computing platform equipped with 96 Intel CPU cores and 256 GB of memory, and parallel computation was utilized to enhance computational efficiency.

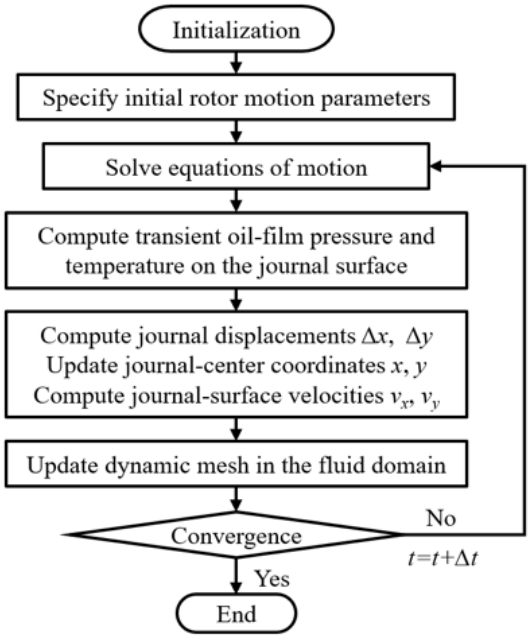

Figure 6. Schematic flowchart of transient journal-motion computation.

3.3. Validation of Computational Model Accuracy

To ensure both computational accuracy and efficiency, several validation procedures were performed in this study, including mesh-independence verification, time-step sensitivity analysis, validation of static bearing characteristics, and verification of journal temperature distribution. Mesh-independence verification was conducted first. Due to the complex mesh structure in the lubricant inlet region, a multizone meshing strategy was adopted. The overlap surfaces between the oil groove and the oil film were defined as interfaces. Because of the small radial dimension of the oil-film region, a sweep method was used to generate hexahedral meshes, and five mesh layers were arranged in the radial direction at the oil-film outlet region. A schematic of the oil-film mesh for the journal bearing is shown in Figure 7. Five different mesh densities were considered, with total cell numbers of 158,000, 286,000, 326,000, 387,000, and 435,000, respectively. The mesh-independence results are presented in Figure 8. As shown, when the mesh number reached approximately 387,000, both the maximum oil-film pressure and the load-carrying capacity exhibited negligible variation. Considering computational efficiency, the mesh with 387,000 cells was therefore adopted for all subsequent simulations.

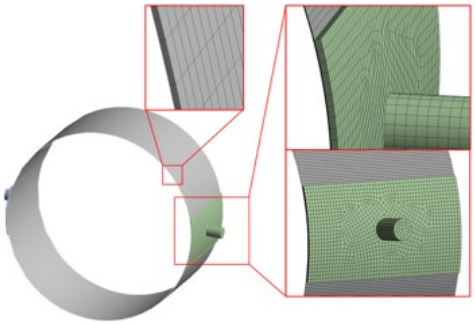

Figure 7. Schematic of the oil-film mesh for the journal bearing.

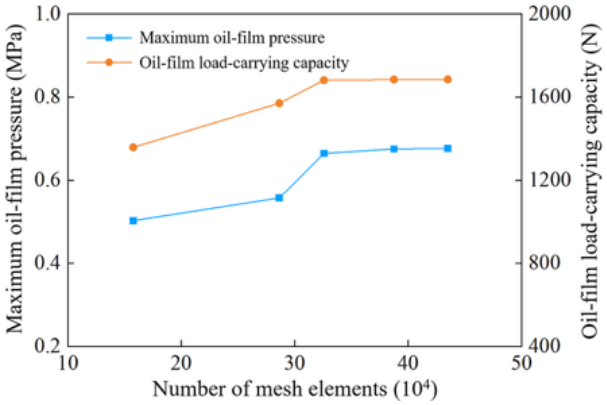

Figure 8. Grid-independence results.

In this study, the thermal effects of the journal were investigated under different whirl ellipticities and whirl frequencies. Because the oil-film flow occurs within an ultra-thin lubrication clearance, an excessively large transient time step may cause numerical oscillations or even divergence, whereas an excessively small time step greatly increases the computational cost. Moreover, the accuracy of the results at different whirl frequencies is highly sensitive to the choice of time step. Therefore, time-step validation is required for each whirl frequency considered. To accurately resolve time-dependent characteristics, the time step must be sufficiently small. Typically, at least 50 time steps per whirl period are required to capture the essential physical features of the solution. For journal whirl motion, the selection of the time step must be compatible with the whirl frequency, and is determined as follows:

$$\Delta t = \frac{1}{t_n f} \tag{21}$$

where Δt is the time step size, t_n is the number of time steps within one whirl period, and f is the journal whirl frequency.

As the journal whirl frequency increases, the numerical solution becomes more susceptible to instability. Therefore, time-step accuracy validation was conducted at a whirl frequency of 200 Hz using a linear whirl orbit with an elliptical eccentricity of 1.0. Table 3 provides the results of this validation. As shown, when the number of time steps per whirl period reached 400, the oil-film force components F_x and F_y became effectively invariant. Accordingly, for all whirl frequencies examined in this study, the number of time steps per period was set to 400.

Table 3. Time-step accuracy verification.

t_n	f (Hz)	Δt	F_x (N)	F_y (N)
50	200	1.00×10^{-4}	−658	1407
250	200	2.00×10^{-5}	−655	1357
400	200	1.25×10^{-5}	−654	1351
800	200	6.25×10^{-6}	−654	1351

To verify the accuracy of the static-characteristic calculation model for the journal bearing proposed in this study, an unsteady dynamic-mesh CFD approach was employed to determine the static equilibrium position of the journal. The bearing model reported in Ref. [36] was adopted as a benchmark to construct the validation case. The journal rotational speed was set to 9550 r/min, and the calculation procedure shown in Figure 6 was followed. The oil-film forces obtained from the CFD solution were substituted into the kinematic Equation (11) to determine the journal velocity and displacement. Through iterative computation, the oil-film forces obtained by integrating the pressure distribution

at each iteration were compared with the applied load. As the solution converges, the horizontal oil-film force F_x approaches zero, while the vertical oil-film force F_y becomes equal in magnitude and opposite in direction to the static bearing load. The journal center gradually converges to a fixed position, which is identified as the static equilibrium position O_j. A comparison between the present results and those reported in the reference literature is given in Table 4. The discrepancies in eccentricity ratio ε and attitude angle θ were 2.0% and 2.3%, respectively, both within the 5% tolerance generally accepted in engineering practice. Therefore, the static-characteristic calculation model adopted in this study was considered to be reliable and sufficiently accurate.

Table 4. Comparison of static equilibrium position results between this study and Ref. [36].

	Eccentricity Ratio ε	Attitude Angle θ (°)
Results from Ref. [36]	0.50	49.82
Results of the present study	0.49	50.99
Relative deviation (%)	2.0	2.3

To validate the accuracy of the temperature-solution model proposed in this study, temperature distributions were computed both with and without considering thermal expansion of the journal and bearing. The inlet oil temperature was set to 50 °C, and the rotational speed was 8000 r/min. The results are shown in Figure 9. As can be seen, the two cases exhibited nearly identical trends. The maximum journal temperature was 74.5 °C when thermal expansion was included and 74.1 °C when it was neglected, corresponding to a relative difference of only 0.5%. Therefore, to improve computational efficiency while maintaining sufficient accuracy, thermal expansion of the journal and bearing was neglected in the present study. Subsequently, the experimental model parameters and boundary conditions reported by Kucinschi [37] were adopted. Numerical simulations were performed using the proposed modeling framework and computational method, and the results were compared with the experimental data. The comparison is presented in Figure 10. As shown, the circumferential temperature distribution predicted by the present model agreed well with the experimental measurements of Kucinschi [37]. The overall trends were consistent, and the circumferential temperature differences remained relatively small. These results demonstrate that the proposed model provides sufficient accuracy in predicting journal temperature distribution characteristics.

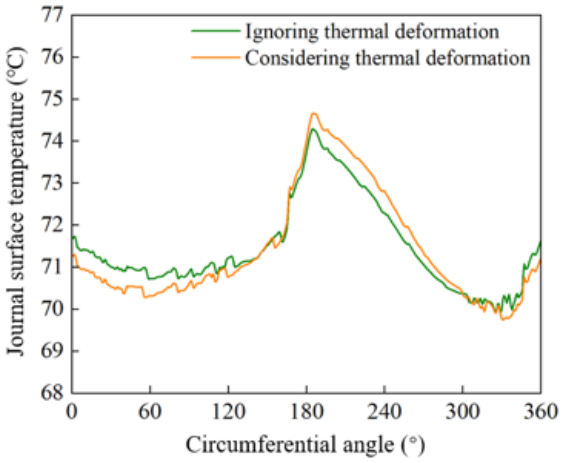

Figure 9. Comparison of circumferential temperature differences computed with and without thermal expansion of the journal and bearing.

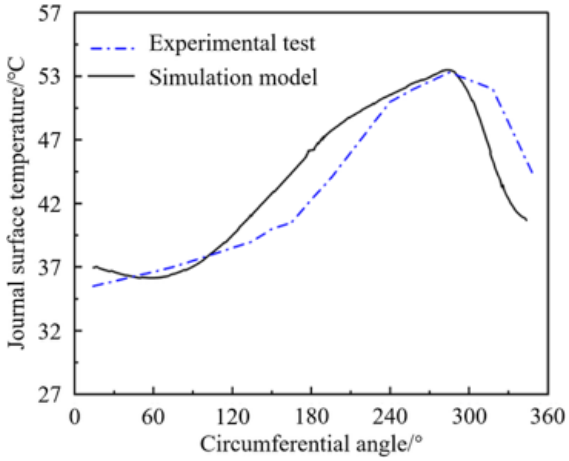

Figure 10. Comparison between the present computed circumferential journal temperature distribution and the experimental results of Kucinschi [37] (ω = 314.16 rad/s, W = 4000 N).

4. Results and Discussion

4.1. Influence of Different Whirl Orbits on Journal Pressure Distribution

This study investigated the effects of different whirl-orbit shapes and whirl frequencies on the dynamic characteristics of journal bearings. Referring to Table 1, six different elliptical eccentricities ε_ω were adopted to characterize the whirl-orbit shape. The rotational speed was set to 8000 r/min, corresponding to a synchronous whirl frequency of 133.3 Hz. Figure 11 presents the time-domain histories of the oil-film forces acting on the journal. Because the whirl amplitude in the fixed x-direction remains constant during forward whirl, only F_x was analyzed for forward whirl. In contrast, during backward whirl, the whirl amplitude in the fixed y-direction remains constant, and therefore only F_y was examined. As shown in Figure 11, at a frequency of 100 Hz, the amplitude of F_x under forward whirl increased with increasing ε_ω. In this case, the journal center underwent small-amplitude circular motion around the bearing center in the same direction as the rotor rotation, generating a stable periodic oil-film force. Under steady conditions, the oil-film force F can be decomposed into horizontal F_x and vertical F_y components. When ε_ω was small, the whirl orbit is nearly circular, and the oil-film thickness varied smoothly with time, resulting in relatively weak pressure fluctuations. As ε_ω increased, the orbit gradually elongated from a circular shape toward a nearly linear trajectory. Consequently, the oil-film thickness underwent periodic compression and expansion along this direction, and the convergent and divergent regions of the oil-film clearance varied more strongly. The resulting pressure vector was dominated by the reaction force along the x-direction, leading to a pronounced increase in pressure-fluctuation amplitude. In contrast, under backward whirl, the journal center was perturbed in the direction opposite to the rotor rotation, and the amplitude of F_y decreased with increasing ε_ω. When the whirl orbit approached a linear form, variations in oil-film thickness were mainly concentrated in the vertical direction. During the downward motion of the journal, the side where a convergent region would normally form instead experienced an increase in oil-film thickness, which reduced the pressure and caused a significant decrease in F_y. Figure 11 also shows a clear phase difference between the journal displacements and the corresponding oil-film forces in the x- and y-directions.

Figure 12 presents the frequency-domain characteristics of the oil-film forces acting on the journal. As the whirl frequency increased, the amplitudes of F_x under forward whirl and F_y under backward whirl both increased progressively. Under forward whirl, the convergent region of the oil-film clearance generated by journal displacement aligned with the direction of journal rotation, jointly amplifying the pressure-fluctuation magnitude.

Consequently, the horizontal oil-film force F_x increased with increasing whirl frequency. Similarly, under backward whirl, the variation in film thickness in the vertical direction became increasingly pronounced with higher whirl frequency, resulting in a greater amplitude of F_y in the frequency domain.

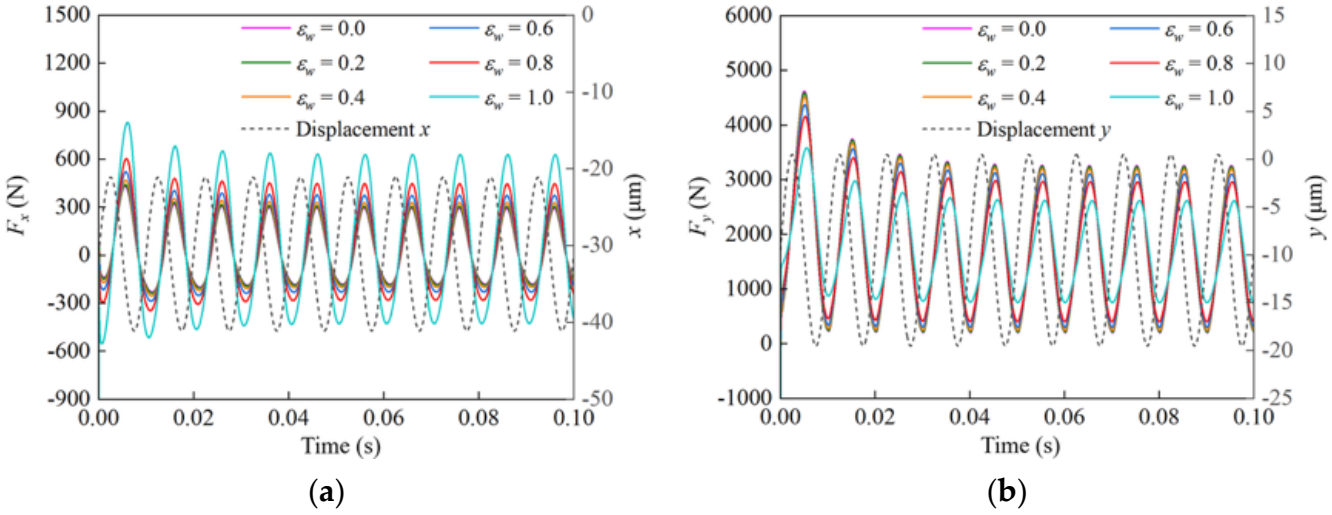

Figure 11. Time-domain oil-film forces acting on the journal: (**a**) f = 100 Hz, forward whirl; (**b**) f = 100 Hz, backward whirl.

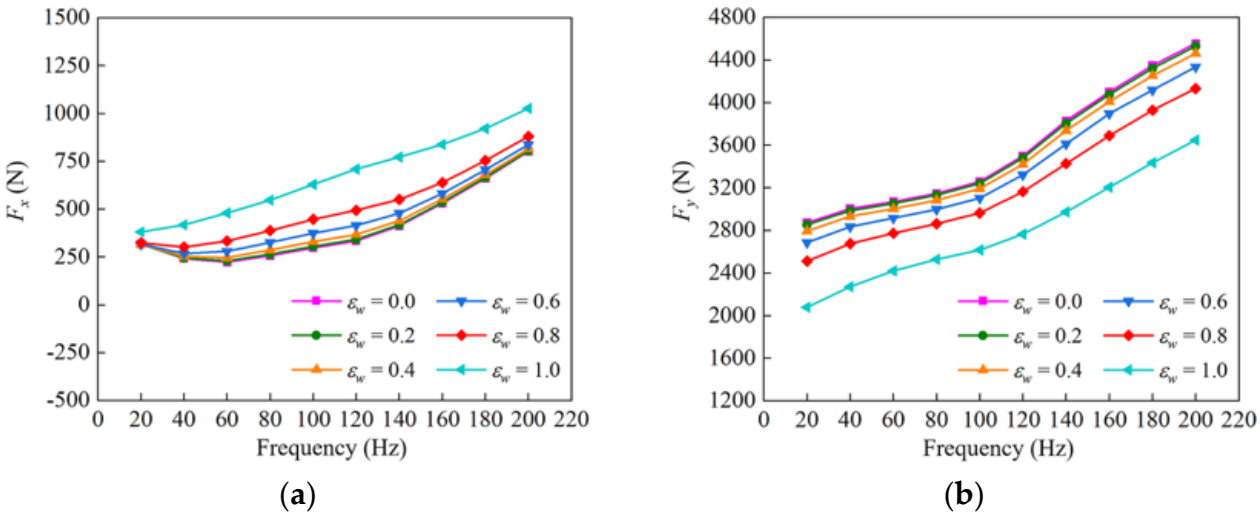

Figure 12. Frequency-domain oil-film forces acting on the journal: (**a**) forward whirl; (**b**) backward whirl.

To further elucidate the mechanism of hydrodynamic pressure buildup in the oil film under different whirl motion and its dominant role in the evolution of thermal effects, the circumferential pressure distribution on the journal surface was examined in conjunction with variations in the film clearance. As shown in Figure 13, under forward whirl, the whirl direction was consistent with the rotor rotation, which markedly enhanced the effective entrainment and transport of lubricant into the convergent wedge region. As a result, a stable and concentrated high-pressure zone formed upstream of the location of minimum film thickness. A clear phase difference existed between the pressure peak and the minimum-clearance position. This upstream shift of the peak is a direct manifestation of the classical hydrodynamic lubrication mechanism: pressure rises rapidly as the clearance decreases in the convergent region, whereas after the minimum-clearance point, the flow enters the divergent region, where pressure decays rapidly and may even drop to low-pressure levels. With increasing whirl frequency, the pressure buildup capability in the

convergent region first decreases and then increases. Under high-frequency whirl, the pressure peak increases and the high-pressure zone becomes more concentrated, indicating that whirl motion can strengthen the wedge effect of the oil film. With respect to elliptical eccentricity, increasing ε_ω amplifies the periodic variation in film thickness, enhancing the wedge-induced hydrodynamic effect in the convergent region and thereby altering the circumferential extent and peak level of the high-pressure zone. Overall, under forward whirl, a high-pressure region forms more readily and exhibits more pronounced localization, providing a direct dynamical basis for the subsequent development of localized high shear and high-temperature regions.

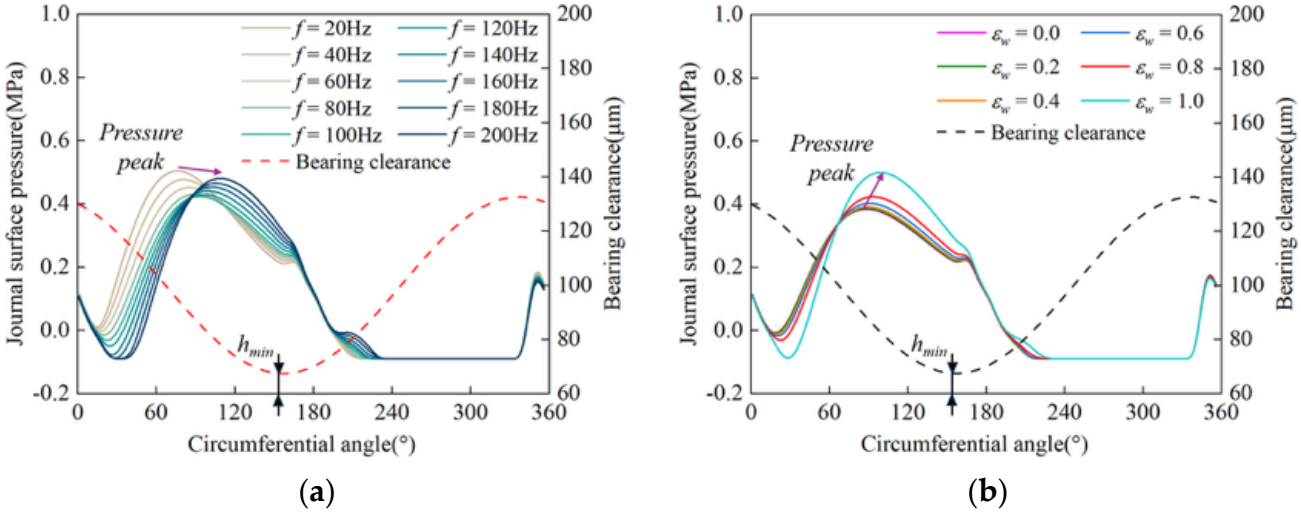

Figure 13. Circumferential pressure distribution on the journal surface under forward whirl for different whirl frequencies and elliptical eccentricities: (**a**) ε_ω = 0.8, forward whirl; (**b**) f = 100 Hz, forward whirl.

In contrast, under backward whirl, the journal motion is opposite to the main rotational direction. As shown in Figure 14, lubricant entrainment is weakened and a convergent wedge structure is difficult to sustain, leading to a substantially reduced high-pressure region and a more diffuse pressure distribution. In this case, even though a minimum-clearance location still exists, the pressure peak responds much more weakly to clearance variation. The pressure field becomes smoother in the circumferential direction and is accompanied by a broader low-pressure region and a stronger tendency toward near-cavitation conditions. With increasing whirl frequency, the pressure level again exhibits a trend of first decreasing and then increasing, but the magnitude of enhancement is significantly smaller than that under forward whirl. This indicates that, under backward whirl, the hydrodynamic pressure buildup mechanism is constrained, and the load capacity is contributed mainly by global shear-driven effects and local transient squeeze effects rather than by a stable wedge-induced hydrodynamic pressure. Although increasing ε_ω can, to some extent, modify the strength of clearance modulation, its ability to increase the pressure peak remains limited when the underlying hydrodynamic mechanism is weakened. These comparisons indicate that the whirl direction determines whether a hydrodynamic wedge can be established and how strongly the pressure field is localized. Whirl frequency and elliptical eccentricity mainly modulate the pressure peak and the extent of the high-pressure region by altering the effective relative velocity and the strength of clearance modulation. The degree of pressure localization is a prerequisite for subsequent shear-stress concentration, localization of viscous dissipation, and the formation of circumferential temperature nonuniformity.

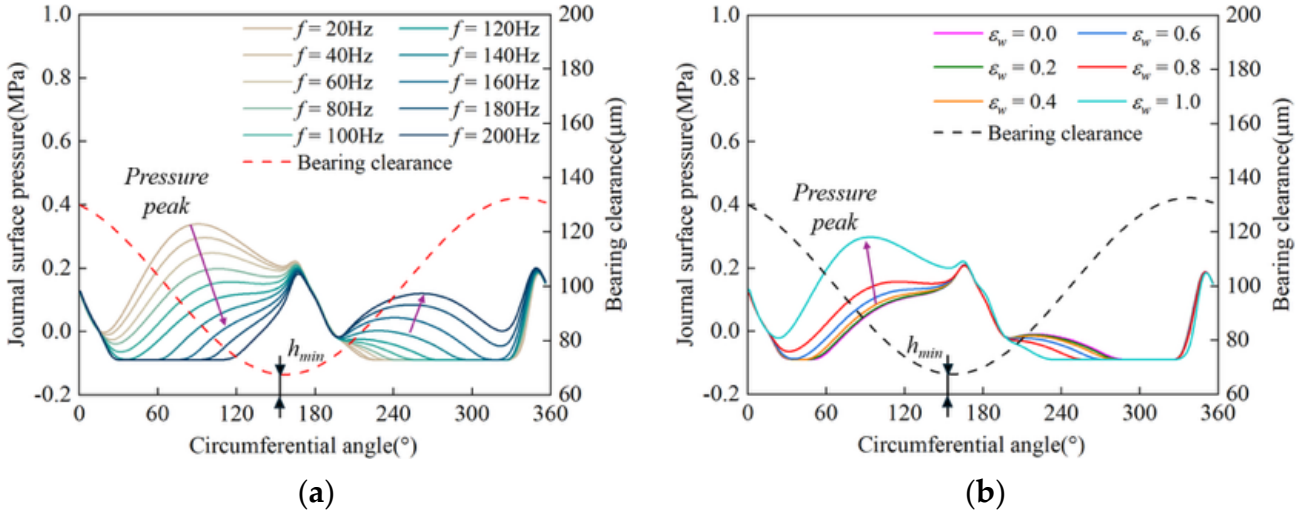

(**a**) (**b**)

Figure 14. Circumferential pressure distribution on the journal surface under backward whirl for different whirl frequencies and elliptical eccentricities: (**a**) ε_ω = 0.8, backward whirl; (**b**) f = 100 Hz, backward whirl.

4.2. Influence of Different Whirl Orbits on Journal Temperature Distribution

As shown in Figure 15, three axial sections were extracted from the journal surface and averaged, and the angular definition followed that illustrated in Figure 1. Figures 16 and 17 present the circumferential temperature distributions on the journal surface under forward and backward whirl, respectively, for different whirl frequencies and elliptical eccentricities. As observed in Figure 16a, under forward whirl, the temperature at the 180° position of the journal decreased continuously with increasing whirl frequency, while the temperature in the 60°~120° region first decreased and then increased. The circumferential angles of 0° and 180° corresponded to the lubricant inlet locations, where the inlet temperature was 50 °C; therefore, a distinct temperature drop appeared downstream of both 0° and 180°. As the elliptical eccentricity ε_ω increased from 0 to 1, the overall circumferential temperature distributions remained similar. Within the 0°~180° range, the journal temperature increased gradually, whereas in the 180°~360° range, it decreased continuously, which is beneficial for reducing the circumferential temperature difference on the journal surface. When ε_ω was large, the whirl orbit tended toward a linear trajectory, resulting in pronounced variations in oil-film thickness and enhanced convective heat transfer. In contrast, when ε_ω was small, the orbit approached a circular shape, the oil-film thickness varied more uniformly, and heat was more likely to accumulate, leading to a larger circumferential temperature difference on the journal surface.



Figure 15. Schematic of journal cross-section.

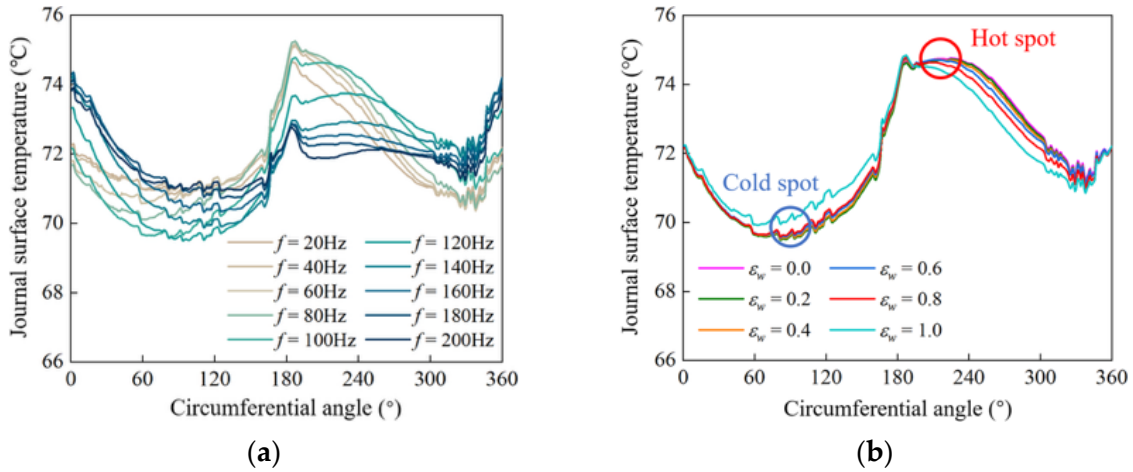

Figure 16. Circumferential distribution of journal-surface temperature under forward whirl for different whirl frequencies and elliptical eccentricities: (**a**) ε_ω = 0.8, forward whirl; (**b**) f = 100 Hz, forward whirl.

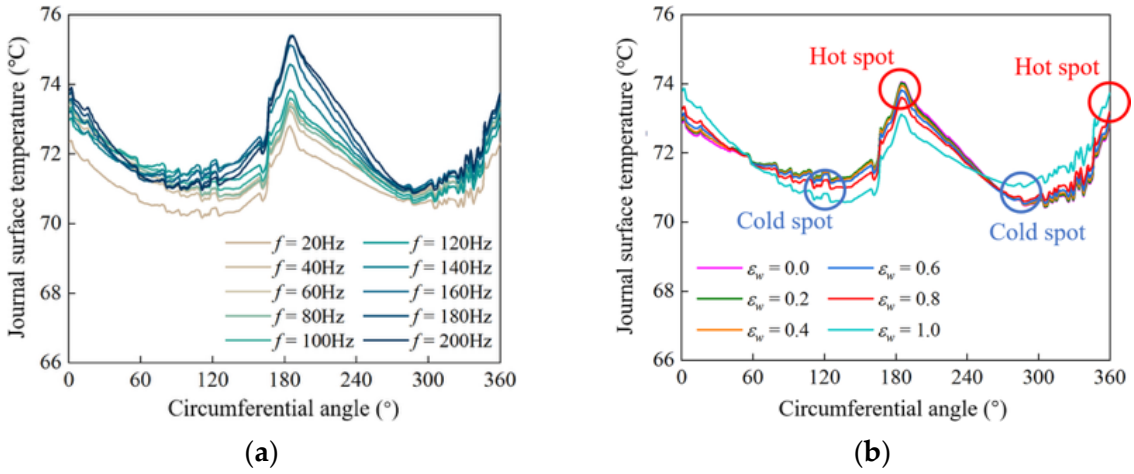

Figure 17. Circumferential distribution of journal-surface temperature under backward whirl for different whirl frequencies and elliptical eccentricities: (**a**) ε_ω = 0.8, backward whirl; (**b**) f = 100 Hz, backward whirl.

As shown in Figure 17, under backward whirl, the temperature near the 180° position on the journal surface increased continuously with increasing whirl frequency, where most of the generated heat tended to accumulate. As the whirl frequency rose, the viscous shear rate within the oil film increased accordingly, intensifying shear-induced heat generation and leading to a pronounced local temperature rise. Under forward whirl, the circumferential temperature distribution on the journal surface was approximately sinusoidal, forming a distinct hot-spot region and a cold-spot region. This corresponded to a clear first-order circumferential temperature pattern, which may induce significant thermal bending of the rotor journal. In contrast, under backward whirl, two hot regions and two cold regions with opposite phases were observed, constituting a second-order circumferential temperature distribution. The two hot regions were approximately 180° out of phase, and the two cold regions exhibited a similar phase separation. Although a circumferential temperature difference still existed, the temperatures at opposite phases were nearly identical, and thus an effective thermal bending moment could not be generated. In this case, rotor vibration instability is more likely caused by the inability of the journal surface to establish an effective convergent oil-film clearance. Therefore, different mitigation strategies should

be adopted for the two distinct whirl modes in order to reduce the likelihood of vibration instability in rotor–bearing systems.

Figure 18 illustrates the circumferential temperature difference of the journal under forward and backward whirl for different elliptical eccentricities and whirl frequencies. Under forward whirl, as the frequency increased from 20 Hz to 200 Hz, the circumferential temperature difference first increased and then decreased. When the frequency lay in the range of 80~100 Hz, the temperature difference reached a maximum value of 5.4 °C. This behavior can be attributed to the enhanced hydrodynamic effect induced by forward whirl. As the frequency increased, the whirl frequency gradually approached the synchronous whirl frequency, intensifying shear deformation and viscous dissipation of the lubricant within the convergent region, which promoted local heat accumulation and led to higher temperature peaks. However, when the frequency further increased beyond approximately 120~160 Hz, the circumferential temperature difference began to decrease. This is because high-frequency forward whirl, combined with rotor rotation, produces a pumping effect within the narrow oil-film clearance, accelerating lubricant flow and alleviating local thermal accumulation. In addition, increasing the elliptical eccentricity slightly reduced the circumferential temperature difference, particularly in the mid-frequency range of 60~100 Hz. As ε_ω increased, the whirl orbit became more elongated, and the temporal variation of oil-film thickness became more pronounced, which weakened the thermal accumulation effect.

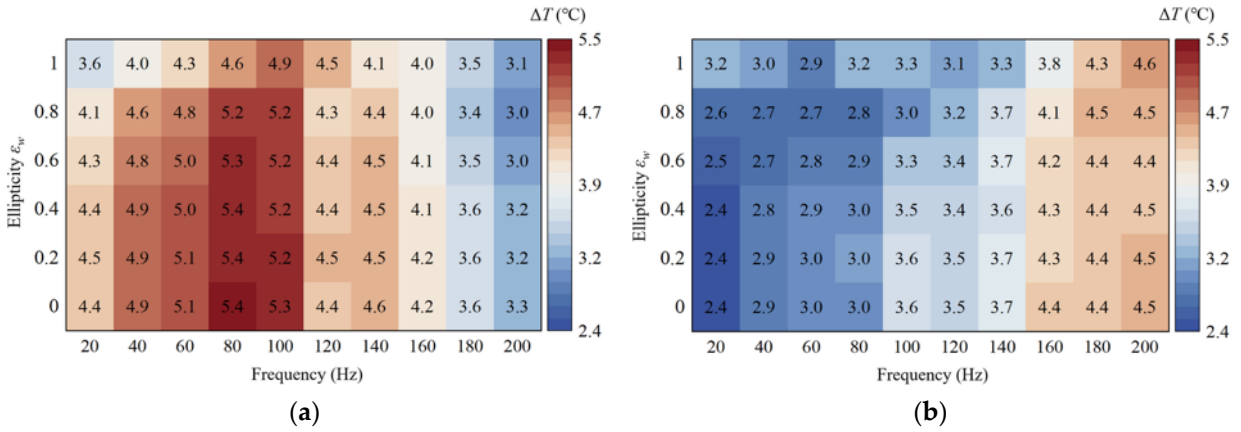

Figure 18. Circumferential temperature difference on the journal surface under different elliptical eccentricities and whirl frequencies: (**a**) forward whirl; (**b**) backward whirl. Under forward whirl, ΔT first increases and then decreases with increasing frequency, reaching a peak in the intermediate-frequency range due to intensified hydrodynamic heating induced by the wedge effect. Increasing ε_ω reduces ΔT by enhancing convective heat transfer. In contrast, under backward whirl, ΔT increases monotonically with frequency and shows weak sensitivity to ε_ω because shear dissipation dominates heat generation.

Under backward whirl, the circumferential temperature difference ΔT increased monotonically with whirl frequency, while showing little sensitivity to variations in the elliptical eccentricity ε_ω. This behavior is mainly attributed to the fact that, during backward whirl, the direction of journal motion is opposite to the lubricant inflow direction. As a result, a blocking effect occurs within the narrow oil-film clearance, weakening the hydrodynamic pressure generated in the convergent region and even leading to the formation of low-pressure or negative-pressure zones. Consequently, the dominant heat-generation mechanism shifted from localized non-uniform viscous shear dissipation in the convergent region to overall shear heating throughout the entire oil-film clearance. As the whirl frequency increased, the shear rate induced by journal motion within the oil film continued to rise, thereby causing a progressive increase in the circumferential temperature difference ΔT.

Figure 19 presents the average journal temperature under forward and backward whirl for different elliptical eccentricities and whirl frequencies. Under forward whirl, the average temperature T_a varied only slightly over the entire ranges of frequency and elliptical eccentricity. In general, a higher frequency and a smaller elliptical eccentricity correspond to a slightly higher average temperature. In forward whirl, heat generation is mainly concentrated in the local convergent wedge region of the oil film and is dominated by localized viscous dissipation. Since the average temperature is obtained by circumferentially averaging the entire journal surface, localized heat accumulation near the 180° region, although producing a pronounced temperature peak, does not result in a significant increase in the overall mean temperature. In contrast, under backward whirl, the average temperature T_a increases monotonically with increasing whirl frequency, and it also shows a slight increase with increasing elliptical eccentricity, although the influence of eccentricity is much weaker than that of frequency. This behavior arises because, as the whirl frequency increases, the overall shear power density within the oil film is enhanced, leading to heat generation over the entire lubrication clearance. As a result, thermal accumulation is no longer confined to a local convergent region but instead elevates the overall temperature level of the oil film, causing a pronounced increase in the average temperature T_a.

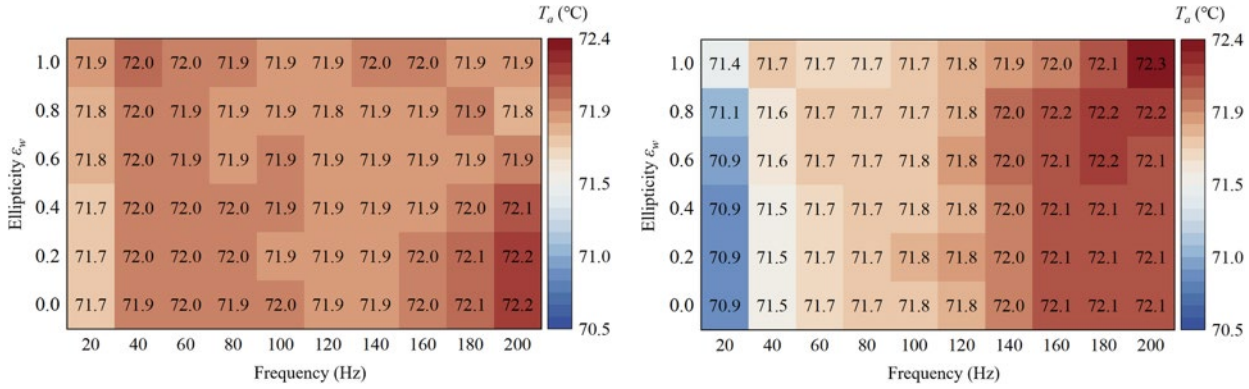

Figure 19. Average journal-surface temperature under different elliptical eccentricities and whirl frequencies: (**a**) forward whirl; (**b**) backward whirl. Under forward whirl, T_a varies only slightly because heat is locally concentrated in the convergent wedge region; a slight increase in ε_ω leads to a reduction in T_a. Under backward whirl, T_a increases monotonically with frequency due to globally distributed shear heating, while the influence of ε_ω remains limited.

Figure 20 shows the temperature contours on the journal surface at a whirl frequency of 100 Hz for different elliptical eccentricities. Under forward whirl, a pronounced circumferential temperature peak formed in the range of 270°~360°, and the extent of this peak region decreased as the elliptical eccentricity ε_ω increased. The cold regions mainly appeared downstream of the lubricant inlet, where intensive mixing between hot and cold oil occurred, forming a distinct "cold groove." Within the convergent wedge clearance, the combined effects of high pressure and small oil-film thickness resulted in large near-wall velocity gradients and strong viscous dissipation, causing heat to accumulate within a limited region. Along the axial direction, a banded temperature pattern was observed, characterized by a relatively cooler midsection and hotter ends. Due to viscous shear, the temperature rise gradually propagated toward both sides, while at the axial ends, the temperature dropped sharply as a result of side leakage cooling. Under backward whirl, the axial temperature-band distribution became smoother and more continuous. Although the axial ends were still affected by side-leakage cooling, the overall temperature gradient was smaller than that observed under forward whirl. Due to the presence of low-pressure

regions and cavitation tendencies, the wedge effect of the oil-film clearance is weakened, leading to a more uniform circumferential convective distribution. As a result, shear heating dominates throughout the oil film, and the temperature field evolves smoothly with the flow. At high whirl frequencies and large elliptical eccentricities, the increase in average temperature reduces lubricant viscosity, thereby decreasing the equivalent stiffness and damping of the bearing and reducing the static load-carrying margin.

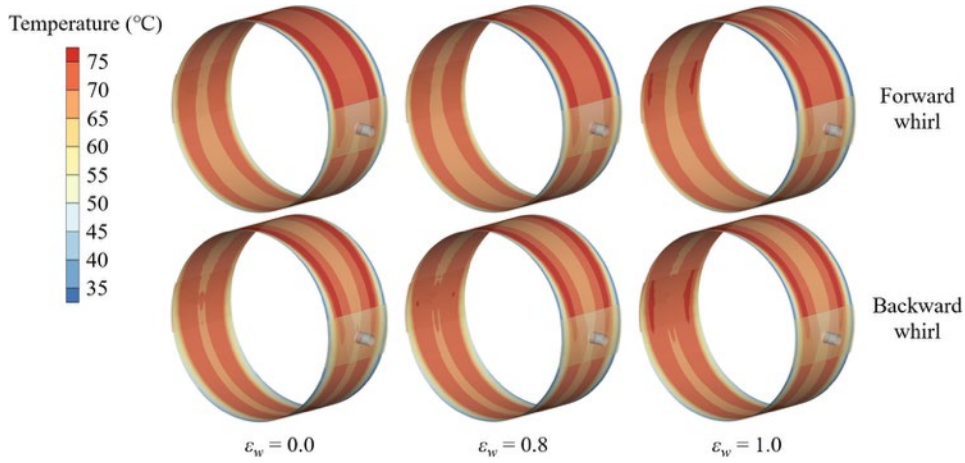

Figure 20. Journal-surface temperature contour maps at a whirl frequency of 100 Hz under forward and backward whirl.

Figure 21 presents the pressure contours on the journal surface at a whirl frequency of 100 Hz for different elliptical eccentricities. Under forward whirl, a distinct localized high-pressure region developed within the convergent zone of the oil film, indicating a pronounced enhancement of the hydrodynamic effect. This behavior arises because the direction of journal whirl coincides with the rotor rotation, which increases the effective relative surface velocity and strengthens the entrainment of lubricant into the convergent wedge region, thereby promoting the formation of a stable hydrodynamic pressure wedge. As the elliptical eccentricity of the whirl orbit increases, the circumferential extent of the high-pressure region further expands and the pressure distribution becomes more stable, reflecting a continuous improvement in the load-carrying capacity of the oil film. In contrast, under backward whirl, the journal motion was opposite to the direction of rotor rotation, resulting in a substantial reduction in the effective relative sliding velocity. Consequently, the entrainment capability of the lubricant was suppressed, and a stable convergent wedge structure could not be effectively established. As a result, the hydrodynamic pressure buildup inside the bearing was significantly weakened, and the pressure distribution became more diffuse. Although the oil-film pressure increased gradually with increasing elliptical eccentricity, its peak value remained considerably lower than that observed under forward whirl. These comparisons demonstrate that the whirl direction plays a dominant role in the hydrodynamic pressure formation mechanism of journal bearings. The enhanced hydrodynamic effect under forward whirl provides the physical basis for localized heat accumulation and the development of first-order circumferential temperature nonuniformity, whereas the weakened pressure response under backward whirl fundamentally explains the limited thermal excitation capability observed in this operating condition.

Figure 22 shows the shear-stress contours on the journal surface at a whirl frequency of 100 Hz for different elliptical eccentricities. Under forward whirl, the journal whirl trajectory was aligned with the direction of rotation, leading to the formation of a stable convergent region ahead of the attitude angle. In this region, the oil-film thickness reached its minimum value, and consequently the maximum wall shear-stress peak developed. As illustrated in

the figure, this high–shear-stress band was mainly distributed in the central region of the bearing. At the bearing ends, side leakage occurred, and because higher pressure existed in the lower part of the bearing, the shear-stress level near the ends decreased. As a result, a distinct axial distribution characterized by higher shear stress in the middle and lower values at both ends was observed in the lower half of the bearing. With increasing elliptical eccentricity, the whirl orbit became progressively more elongated, and the journal surface experienced increasingly pronounced pressure fluctuations. Accordingly, the high-shear-stress band in the lower half of the bearing expanded gradually. Under backward whirl, the shear-stress peaks were also mainly concentrated at locations where the oil-film thickness was minimal. Compared with forward whirl, the distribution range was broader, but the peak magnitude was lower. As elliptical eccentricity increased, the shear-stress distribution in the lower half of the journal expanded, exhibiting a trend similar to that observed under forward whirl. Although the overall shear-stress level increased slightly, it remained lower than that under forward whirl. This is because the pressure peaks in backward whirl are intrinsically weakened, and even when the whirl trajectory becomes more elongated, the enhancement of local shear stress remains limited.

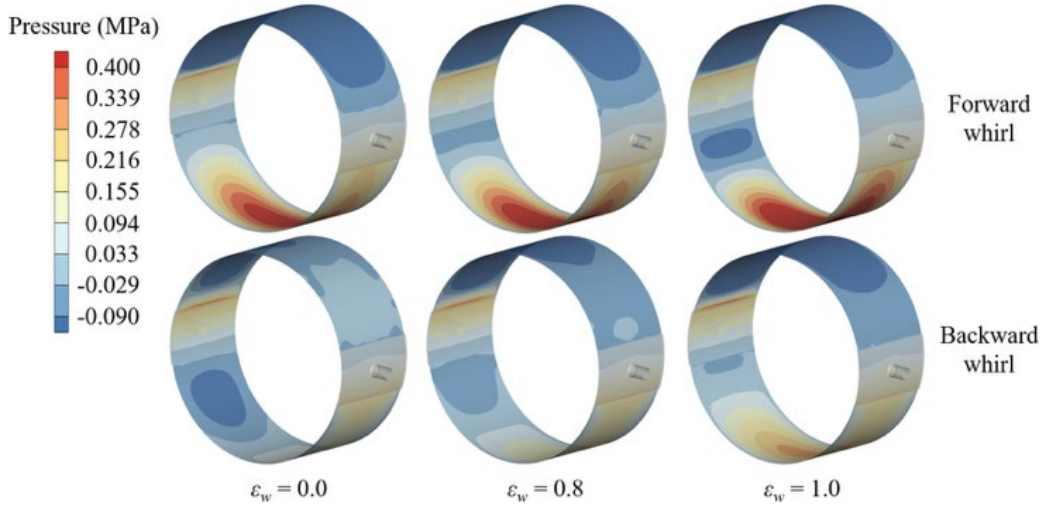

Figure 21. Journal-surface pressure contour maps at a whirl frequency of 100 Hz under forward and backward whirl.

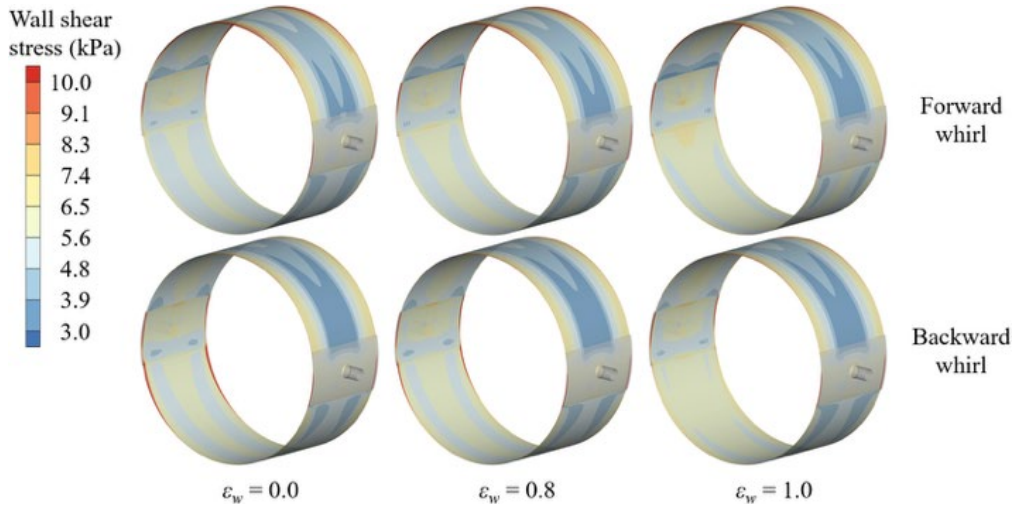

Figure 22. Journal-surface shear-stress contour maps at a whirl frequency of 100 Hz under forward and backward whirl.

5. Conclusions

This study developed a thermal analysis model for journal bearings that accounts for journal whirl trajectories, based on computational fluid dynamics and an unsteady structured dynamic-mesh updating method. The whirl-orbit shape was characterized using the elliptical eccentricity, and the effects of different eccentricities and whirl frequencies under forward and backward whirl conditions on heat-generation mechanisms and circumferential temperature distributions were systematically investigated. The main conclusions are summarized as follows:

1. At a whirl frequency of 100 Hz, the whirl amplitude of the oil-film force F_x under forward whirl increases with increasing elliptical eccentricity, whereas under backward whirl, the amplitude of F_y decreases with increasing elliptical eccentricity. As whirl frequency increases, both F_x in forward whirl and F_y in backward whirl increase progressively.
2. Forward and backward whirl exhibit fundamentally different temperature-distribution characteristics. Under forward whirl, the journal motion is aligned with rotor rotation, significantly strengthening the convergent wedge effect of the oil film and forming localized regions of high pressure and high shear. This condition readily induces a first-order circumferential temperature pattern, characterized by a single hot spot and a single cold spot, with a strong potential to generate pronounced thermal bending of the journal. In contrast, under backward whirl, the journal motion opposes the main lubricant flow direction, markedly weakening hydrodynamic pressure buildup and producing a more diffuse pressure field. The resulting temperature distribution exhibits a second-order circumferential pattern with two hot spots in opposite phases, substantially reducing the capability to induce effective thermal bending.
3. The elliptical eccentricity plays a key role in modulating the journal temperature field by altering the whirl-orbit geometry. As elliptical eccentricity increases, the whirl trajectory evolves from a nearly circular shape toward an elongated form, significantly amplifying the periodic variation of oil-film thickness and enhancing convective heat transfer. This process mitigates local thermal accumulation. Under forward whirl, this effect is particularly pronounced, leading to a reduction in circumferential temperature difference with increasing elliptical eccentricity. Under backward whirl, however, where global shear heating dominates, variations in elliptical eccentricity exert only a limited influence on both circumferential temperature difference and average temperature.
4. Whirl frequency is a critical parameter governing the intensity of thermal effects. Under forward whirl, increasing frequency enhances hydrodynamic pressure and localized viscous dissipation, leading to noticeable heat accumulation in an intermediate frequency range. Consequently, the circumferential temperature difference first increases and then decreases, reaching a peak value of 5.4 °C in the mid-frequency band (80~100 Hz). At higher frequencies, accelerated oil-film flow strengthens convective heat transfer and alleviates local thermal buildup. Under backward whirl, journal temperature is primarily controlled by the overall shear rate; as whirl frequency increases, the shear power density within the oil film rises continuously, resulting in monotonic increases in both circumferential temperature difference and average temperature.
5. Installation eccentricity introduces a global offset of the bearing clearance, altering the location of the convergent wedge and the minimum film thickness, thereby causing the migration and intensification of pressure peaks and high shear-dissipation regions. An increase in eccentricity generally reduces the minimum film thickness and enhances local velocity gradients, leading to more concentrated hot spots and larger circumferential temperature differences, while changes in the eccentricity direction result in an overall shift of the hot-spot angular position together with the pressure

peak. This effect is more pronounced under forward whirl, where the hydrodynamic wedge and the associated localization of thermal sources are stronger. Future work may jointly parameterize installation eccentricity and whirl trajectories to quantify the sensitivity of circumferential temperature difference and hot-spot phase to the magnitude and direction of eccentricity.

Author Contributions: Conceptualization, Q.Y. and Y.L.; Methodology, Y.L.; Software, Y.L.; Validation, Y.L.; Formal analysis, Q.Y.; Investigation, Y.L.; Resources, Q.Y.; Data curation, Y.L.; Writing—original draft preparation, Y.L.; Writing—review and editing, Y.L., X.L., T.Y. and Q.Y.; Visualization, X.L. and T.Y.; Supervision, Q.Y.; Project administration, Q.Y.; Funding acquisition, Q.Y. All authors have read and agreed to the published version of the manuscript.

Funding: This research was funded by the National Natural Science Foundation of China (12372057).

Data Availability Statement: The original contributions presented in this study are included in the article. Further inquiries can be directed to the corresponding author.

Conflicts of Interest: The authors declare no conflicts of interest.

Abbreviations

The following abbreviations are used in this manuscript:

a	Semi-minor axis of whirl orbit
b	Semi-major axis of whirl orbit
c	Radial clearance
c_j	Focal distance of elliptical journal orbit
$C_{F,cond}$	Empirical condensation coefficient
$C_{F,evap}$	Empirical evaporation coefficient
c_p	Specific heat capacity at constant pressure
d_c	Thickness of the supply groove
D	Bearing width
D_{in}	Diameter of the supply hole
e	Mass eccentricity of journal
f	Journal whirl frequency
F_x	Oil-film force component in x-direction
F_y	Oil-film force component in y-direction
k	Thermal conductivity of lubricant
l_{in}	Length of the supply hole
M	Effective journal mass supported by bearing
O	Bearing center
O_j	Journal-center location
O_m	Journal mass center
p_{cav}	Cavitation pressure
p_{in}	Supply-oil pressure
R_1	Bearing radius
R_2	Journal radius
t	Time
T	Lubricant temperature
T_0	Supply-oil temperature
t_n	Number of time steps per whirl period
Δt	Time-step size
α_μ	Temperature–viscosity coefficient
ε	Eccentricity ratio
ε_ω	Elliptical eccentricity of journal orbit

μ	Dynamic viscosity of lubricant
μ_0	Initial dynamic viscosity at supply temperature
ρ	Density of lubricating oil
θ	Attitude angle
θ_{in}	Circumferential angle of the supply groove
ω	Rotor rotational speed
Ω	Whirl angular velocity

References

1. Shin, D.; Suh, J.; Palazzolo, A. Parametric Study of Flexure Pivot Bearing Induced Thermal Bow-Rotor Instability (Morton Effect). *J. Tribol.* **2022**, *144*, 071801. [CrossRef]
2. Shin, D.; Palazzolo, A.; Tong, X. Squeeze Film Damper Suppression of Thermal Bow-Morton Effect Instability. *J. Eng. Gas Turbines Power* **2020**, *142*, 121013. [CrossRef]
3. Codrignani, A.; Savio, D.; Magagnato, F.; Frohnapfel, B. A Scaling Parameter for Pressure Losses and Thermal Effects in Lubricant Flows with Viscous Dissipation. *Tribol. Int.* **2017**, *113*, 238–244. [CrossRef]
4. Gomiciaga, R.; Keogh, P.S. Orbit Induced Journal Temperature Variation in Hydrodynamic Bearings. *J. Tribol.* **1999**, *121*, 77–84. [CrossRef]
5. Childs, D.W.; Saha, R. A New, Iterative, Synchronous-Response Algorithm for Analyzing the Morton Effect. *J. Eng. Gas Turbines Power* **2012**, *134*, 072501. [CrossRef]
6. Dal, A.; Sahin, M.; Kilic, M. A Thermohydrodynamic Performance Analysis of a Fluid Film Bearing Considering with Geometrical Parameters. *J. Therm. Eng.* **2023**, *9*, 1604–1617. [CrossRef]
7. Yu, X.; Shao, M.; Yang, X.; Lin, Y.; Lan, Z.; Li, L.; Li, E.; Dai, R.; Jia, W.; Wang, J.; et al. Advances in the Investigation of Thermal Characteristics of Hydrostatic Bearing Spindle: An Overview. *J. Therm. Anal. Calorim.* **2025**, *150*, 3139–3171. [CrossRef]
8. Wang, L.; Geng, H.; Zhang, W.; Ge, X.; He, M. Effect of Ellipticity on Cavitation Mechanism and Thermal Effect of Elliptical Journal Bearings. *Tribol. Online* **2021**, *16*, 279–285. [CrossRef]
9. Peixoto, T.F.; Alves, D.S.; da Silva Tuckmantel, F.W.; Daniel, G.B.; Machado, T.H.; Cavalca, K.L. Effect of Thermal Boundary Conditions on Dynamic Characteristics of Multi-Lobed Bearings. *Mech. Mach. Theory* **2022**, *172*, 104787. [CrossRef]
10. Suh, J.; Palazzolo, A. Three-Dimensional Thermohydrodynamic Morton Effect Simulation—Part I: Theoretical Model. *J. Tribol.* **2014**, *136*, 031706. [CrossRef]
11. Suh, J.; Palazzolo, A. Three-Dimensional Thermohydrodynamic Morton Effect Analysis—Part II: Parametric Studies. *J. Tribol.* **2014**, *136*, 031707. [CrossRef]
12. Lu, D.; Zhu, Z.; Lu, J. Characteristic Analysis of Bump Foil Gas Bearing Under Multi-Physical Field Coupling. *Appl. Sci.* **2025**, *15*, 7584. [CrossRef]
13. Skulic, A.; Milojevic, S.; Maric, D.; Ivanovic, L.; Krstic, B.; Radojkovic, M.; Stojanovic, B. The Impact of Lubricant Viscosity and Materials on Power Losses and Efficiency of Worm Gearbox. *Teh. Vjesn. Tech. Gaz.* **2022**, *29*, 1853–1860. [CrossRef]
14. *ISO-7902-1-2020*; ISO Hydrodynamic Plain Journal Bearings Under Steady-State Conditions—Circular Cylindrical Bearings—Part 1: Calculation Procedure. International Organization for Standardization: Geneva, Switzerland, 2020.
15. Taheripour, S.; Saffarian, M.R.; Daneh-Dezfuli, A. Heat Transfer Simulation in an Industrial Journal Bearing Using VOF Method. *J. Braz. Soc. Mech. Sci. Eng.* **2019**, *41*, 248. [CrossRef]
16. Rezvanpour, A.; Miller, R.E. Scaling Analysis as a Tool to Validate CFD Simulation of a Lubricant Flow in the Bearing Housing of a Gas Turbine. *Therm. Sci. Eng. Prog.* **2022**, *36*, 101513. [CrossRef]
17. Fan, B.; Liu, Y.; Liu, H. Static Characteristics Analysis of Offset-Halves Journal Bearings with CFD Method Considering Turbulence and Thermal Effects. *Ind. Lubr. Tribol.* **2026**, *78*, 123–133. [CrossRef]
18. Li, S.; Lin, X.; Jiang, S. A Lubrication Model for Bubbly Oil Lubrication with Interfacial Effect and Thermal Effect Using the Theory of Multiphase Mixtures. *Friction* **2024**, *12*, 271–290. [CrossRef]
19. Wei, C.; Wang, W.; Liao, G.; Zhao, H.; Xu, J. Research on Two-Phase Thermo-Hydrodynamic Lubrication Performance Considering Bubble Dynamics. *Tribol. Int.* **2023**, *190*, 109040. [CrossRef]
20. Sun, D.; Li, S.; Fei, C.; Ai, Y.; Liem, R.P. Investigation of the Effect of Cavitation and Journal Whirl on Static and Dynamic Characteristics of Journal Bearing. *J. Mech. Sci. Technol.* **2019**, *33*, 77–86. [CrossRef]
21. Bhat, J.A.; Harmain, G.A.; Najar, F.A. Alleviating Thermal Challenges in Hydrodynamic Bearings: A Novel Approach through Thrust Bearing Pads with Embedded Cooling Circuitry and Deep Recess. *Tribol. Int.* **2024**, *194*, 109438. [CrossRef]
22. Bhat, J.A.; Harmain, G.A.; Wani, M.F.; Sehgal, R.; Najar, F.A. Performance Enhancement of Hydrodynamic Thrust Bearings: Investigating Cooling Strategies, Deep Recesses, and Textured Surfaces. *Tribol. Int.* **2025**, *211*, 110877. [CrossRef]

23. Li, M.; Gu, C.; Pan, X.; Zheng, S.; Li, Q. A New Dynamic Mesh Algorithm for Studying the 3D Transient Flow Field of Tilting Pad Journal Bearings. *Proc. Inst. Mech. Eng. Part J J. Eng. Tribol.* **2016**, *230*, 1470–1482. [CrossRef]
24. Hagemann, T.; Schwarze, H. Theoretical and Experimental Analyses of Directly Lubricated Tilting-Pad Journal Bearings with Leading Edge Groove. *J. Eng. Gas Turbines Power* **2019**, *141*, 051010. [CrossRef]
25. Yang, J.; Palazzolo, A. Three-Dimensional Thermo-Elasto-Hydrodynamic Computational Fluid Dynamics Model of a Tilting Pad Journal Bearing—Part I: Static Response. *J. Tribol.* **2019**, *141*, 061702. [CrossRef]
26. Yang, J.; Palazzolo, A. Three-Dimensional Thermo-Elasto-Hydrodynamic Computational Fluid Dynamics Model of a Tilting Pad Journal Bearing—Part II: Dynamic Response. *J. Tribol.* **2019**, *141*, 061703. [CrossRef]
27. Yang, J.; Palazzolo, A. Deep Convolutional Autoencoder Augmented CFD Thermal Analysis of Bearings with Inter Pad Groove Mixing. *Int. J. Heat Mass Transf.* **2022**, *188*, 122639. [CrossRef]
28. Yang, J.; Palazzolo, A. Morton Effect Prediction with Validation Using a CFD Based CNN for Pad Inlet Temperatures. *Mech. Syst. Signal Process.* **2023**, *185*, 109827. [CrossRef]
29. Yang, J.; Palazzolo, A. Tilt Pad Bearing Distributed Pad Inlet Temperature with Machine Learning-Part I: Static and Dynamic Characteristics. *J. Tribol. Trans. Asme* **2022**, *144*, 061801. [CrossRef]
30. Yang, J.; Palazzolo, A. Tilt Pad Bearing Distributed Pad Inlet Temperature with Machine Learning—Part II: Morton Effect. *J. Tribol.* **2022**, *144*, 061802. [CrossRef]
31. Gheller, E.; Vardhan Reddy, V.; Koyyalamudi, S.; Chatterton, S.; Panara, D.; Pennacchi, P. Tilting Pad Journal Bearing Computational Fluid Dynamic Parametric Modeling for New Energy Transition Challenges. *J. Eng. Gas Turbines Power* **2024**, *146*, 041019. [CrossRef]
32. Xia, P.; Jin, X.; Song, W.; Liang, Y.; Xu, S.; Liu, J.; Liu, Z.; Ma, W. A Novel Transient Computational Fluid Dynamics-Fluid–Structure Interaction Model for the Pad Adaptive Motion and Rotordynamic Coefficients of Hybrid Porous Tilting Pad Bearings. *Proc. Inst. Mech. Eng. Part J J. Eng. Tribol.* **2024**, *238*, 615–637. [CrossRef]
33. Sakai, K.; Miyagawa, K.; Mariotti, A.; Pasini, A. Prediction of Static Characteristics of Cryogenic Hybrid Journal Bearing for Reusable Pump-Fed Liquid Rocket Engine by Computational Fluid Dynamics Simulation. *Phys. Fluids* **2025**, *37*, 035189. [CrossRef]
34. Guo, C.; Li, P.; Li, X.; Chen, Y.; Zhang, H.; Gu, F. Thermo-Hydrodynamic Performance of Journal Bearings under Water Contamination of Lubricants Considering Rheological and Thermal Effects. *Phys. Fluids* **2025**, *37*, 093606. [CrossRef]
35. Tong, X.; Palazzolo, A. Measurement and Prediction of the Journal Circumferential Temperature Distribution for the Rotordynamic Morton Effect. *J. Tribol.* **2018**, *140*, 031702. [CrossRef]
36. Guo, Z.; Hirano, T.; Kirk, R.G. Application of CFD Analysis for Rotating Machinery—Part I: Hydrodynamic, Hydrostatic Bearings and Squeeze Film Damper. *J. Eng. Gas Turbines Power* **2005**, *127*, 445–451. [CrossRef]
37. Kucinschi, B.; Fillon, M. An Experimental Study of Transient Thermal Effects in a Plain Journal Bearing. *J. Tribol.* **1999**, *121*, 327–332. [CrossRef]

Disclaimer/Publisher's Note: The statements, opinions and data contained in all publications are solely those of the individual author(s) and contributor(s) and not of MDPI and/or the editor(s). MDPI and/or the editor(s) disclaim responsibility for any injury to people or property resulting from any ideas, methods, instructions or products referred to in the content.